JACS
JOURNAL OF THE AMERICAN CHEMICAL SOCIETY
pubs.acs.org/JACS
Article

Interfacial Coupling of Perfluorooctanoic Acid Defluorination with Chromium(VI) Reduction in Aqueous Microdroplets

Xiaoke Ma, Yuliang Li,* Ronghao Wu, Min Wang, Jinsong Liu, Longgang Chu, Xiaolei Wang, and Dongmei Zhou*

Cite This: https://doi.org/10.1021/jacs.6c13880
Read Online
ACCESS | Metrics & More | Article Recommendations | Supporting Information

ABSTRACT: Per- and polyfluoroalkyl substances (PFAS) and hexavalent chromium (Cr(VI)) frequently coexist in industrial waters, but their contrasting redox requirements complicate simultaneous remediation. Here we show that aqueous microdroplets transform this apparent incompatibility into cooperative interfacial reactivity. At the air−water interface, perfluorooctanoic acid (PFOA) and Cr(VI) undergo mutually promoted transformation under ambient conditions. Cr(VI) increases PFOA defluorination by approximately 63%, whereas PFOA enhances Cr(VI) reduction by approximately 41%. Mechanistic analyses identify an oxygen-coupled interfacial redox network in which O_2-derived peroxides, H_2O_2 turnover and Cr-mediated radical generation maintain the flux of reactive intermediates. Molecular dynamics simulations and density functional theory calculations indicate that PFOA spontaneously enriches at the interface and reorganizes the ionic environment to promote K^+-mediated co-localization of Cr(VI). This association electronically activates the headgroup-proximal C−F bond and, together with interfacial confinement, reduces the α-C−F cleavage barrier from 2.80 to 1.39 eV. Together, these findings reveal how microdroplet interfaces spatially and electronically coordinate organofluorine bond cleavage with metal reduction, providing a framework for cooperative remediation of complex contaminant mixtures.

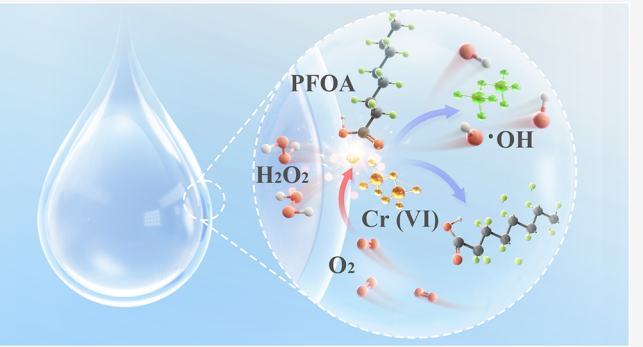

INTRODUCTION

Per- and polyfluoroalkyl substances (PFAS), widely used in nonstick coatings, surfactant formulations, firefighting foams, and fluoropolymer manufacturing, are now recognized as highly persistent anthropogenic contaminants.[1,2] Perfluorooctanoic acid (PFOA), a representative long-chain perfluorinated carboxylate, epitomizes this persistence: its densely fluorinated carbon backbone resists transformation under ambient aqueous conditions, and effective degradation requires activation of otherwise inert C−F bonds.[3−6] PFOA and related fluorinated surfactants have historically been used as mist suppressants in chromium electroplating, and consequently persist alongside hexavalent chromium (Cr(VI)) in effluents from electroplating and metal-finishing operations.[7,8] Cr(VI) is itself a redox-active inorganic contaminant that poses a distinct but equally relevant remediation challenge.[9] Whereas PFOA remediation centers on C−F bond activation,[10,11] Cr(VI) detoxification is governed by oxidation-state control; reduction to Cr(III) generally lowers environmental risk by shifting chromium speciation toward less soluble and less bioavailable forms. This environmental linkage makes PFAS-Cr(VI) systems a relevant organofluorine−metal contaminant pair, particularly in electroplating-related waste streams and chromium-associated exposure scenarios where PFAS and Cr species can coexist.[12] Despite this connection, PFAS degradation and Cr(VI) reduction have largely been investigated as separate remediation processes, leaving their transformation behaviors and pathways under coexisting conditions poorly understood.[13−15]

The key challenge, therefore, is not simply whether PFOA and Cr(VI) can be transformed in the same aqueous system, but whether their distinct transformation pathways can be made mutually reinforcing rather than competitive. PFOA degradation proceeds through electron-mediated and radical-mediated pathways that initiate C−F bond activation and drive stepwise chain transformation, with gas−liquid interfacial environments recently emerging as active sites for PFOA activation.[16−18] In contrast, Cr(VI) reduction requires sustained multi-electron transfer and can itself modulate oxygen-derived radical chemistry.[19−21] When both processes operate simultaneously, they may compete for shared reducing equivalents, radical intermediates, or interfacial reaction space, leading to mutual

Received: July 6, 2026
Revised: August 28, 2026
Accepted: August 31, 2026

inhibition. Alternatively, if one contaminant reshapes the reactive-species flux or local electronic environment in a manner that facilitates the transformation of the other, the two processes may become chemically complementary rather than antagonistic. In homogeneous bulk water, such proximity is difficult to maintain because short-lived intermediates are rapidly diluted, quenched, or spatially separated from surface-active contaminants. A confined interfacial microenvironment that concentrates reactants while sustaining localized charge separation and radical flux could therefore provide a route to cooperative redox transformation.

Aqueous microdroplets offer precisely such a microenvironment. Over the past decade, microdroplets have emerged as reactive media in which chemical transformations can proceed with kinetic and thermodynamic behavior distinct from those in bulk solution.[22,23] Numerous studies report rate enhancements of several orders of magnitude at the air−water interface of micron-sized droplets.[24,25] These phenomena are generally attributed to a unique constellation of factors: interfacial structural asymmetry, intense localized electric fields,[26,27] incomplete solvation,[28,29] and remarkably high surface-to-volume ratios.[30] For solute-containing microdroplets, these interfacial features can act collectively: surface-active molecules may become enriched near the boundary, adsorbed reactants may experience altered solvation and polarization, and charge-transfer events may occur within a confined region rather than throughout the bulk phase.[31,32] Such spatial organization provides a plausible basis for sustaining reactive-intermediate fluxes that are difficult to maintain in homogeneous aqueous solution.

For the present problem, the most relevant feature of microdroplets is their capacity to support interfacial redox chemistry.[33,34] Air−water interfaces have been proposed to promote oxygen-coupled reactive processes through charge asymmetry and electron-transfer events,[35,36] although the microscopic origin and generality of spontaneous reactive oxygen species (ROS) formation in pristine water droplets remain under active discussion.[37] In solute-containing microdroplets, reactive-species fluxes are shaped by interfacial enrichment, dissolved O_2, and the redox properties of the solutes, providing a chemically tunable setting for probing coupled transformations.[38,39] Whether aqueous microdroplets can spatially and electronically organize PFOA transformation and Cr(VI) reduction into a cooperative redox network, rather than merely hosting them as independent or competing reactions, has not been tested.[40−42]

Herein, we investigate the coupled transformation of PFOA and Cr(VI) in aqueous microdroplets, with the aim of determining whether the air−water interface can organize C−F bond activation and Cr(VI) reduction into a cooperative, mutually reinforcing redox process. Rather than treating PFAS degradation and Cr(VI) reduction as independent remediation pathways, this study focuses on how interfacial solute organization, reactive intermediate generation, chromium-mediated redox cycling, and electronic structure reorganization converge within a confined air−water microenvironment. Through integrated experimental and theoretical analysis, we seek to elucidate the molecular basis of microdroplet-organized redox coupling. More broadly, this work tests the concept that confined air−water interfaces act as active redox-organizing media that support the concurrent and mutually promoted transformation of mechanistically distinct contaminants, advancing microdroplet chemistry beyond reaction acceleration toward cooperative redox orchestration.

MATERIALS AND METHODS

Experimental Setup

The aqueous microdroplet reaction system consisted of an ultrasonic atomization device and a sealed reaction chamber placed in a room-temperature water bath. Microdroplets were generated from the reaction solution within the sealed chamber by ultrasonic atomization and collected at predetermined reaction times for chemical analysis. Unless otherwise specified, all reactions were conducted at room temperature under ambient air without external light irradiation, added oxidants, or applied potential. To distinguish bulk-phase ultrasonic cavitation from the effects associated with microdroplet formation, bulk-phase sonication controls were performed by slightly adjusting the reactor angle so that ultrasonic cavitation occurred within the bulk liquid without producing visible atomization. These controls were conducted using the same solution composition, reaction volume, ultrasonic operating settings, and reaction time as the corresponding microdroplet experiments. For droplet size characterization, freshly generated microdroplets were deposited onto hydrophobically coated glass slides to minimize spreading and substrate-induced deformation, followed by optical microscopy imaging and ImageJ analysis. The schematic and photographs of the experimental setup are shown in Figure S1.

Experimental Procedures

In a typical experiment, 6 mL of the reaction solution was loaded into the 20 mL headspace vial, which served as the microdroplet reaction chamber. Unless otherwise specified, the initial PFOA concentration was 5 $mg{\cdot}L^{-1}$, and the Cr(VI) concentration was varied according to the experimental design. Concentration-dependent transformation behavior was evaluated through additional experiments performed at different initial PFOA concentrations, as described in the Supporting Information (Figure S4). For atmosphere-controlled experiments, the reaction solution and the sealed headspace were purged with air, N_2, or O_2 prior to ultrasonic atomization. Unless otherwise specified, all control experiments followed the same procedure.

Analysis Methods

Detailed procedures for the quantitative analysis of PFOA, identification of transformation products, and determination of fluoride, total organic carbon, and residual Cr(VI) are provided in Text S2. Reactive oxygen species were detected by electron paramagnetic resonance spectroscopy (A300-6/1, Bruker), DMPO was employed as the spin-trapping agent for $^{\bullet}OH$-related radicals. Electron paramagnetic resonance (EPR) measurements were performed at room temperature with the following parameters: center field, 3475 G; sweep width, 100 G; microwave frequency, 9.42 GHz; microwave power, 10 mW; modulation amplitude, 1.0 G; and modulation frequency, 100 kHz. $^{\bullet}OH$ and H_2O_2 were further quantified using benzoic acid and the Amplex Red/horseradish peroxidase assay, respectively.[43] Vibrational changes of PFOA and PFOA-Cr(VI) microdroplets were probed by in situ Fourier transform infrared spectroscopy (TENSOR 27, Bruker) equipped with a ZnSe attenuated total reflectance accessory.[44] The interfacial electric field was probed by in situ surface-enhanced Raman spectroscopy (XploRA Plus, HORIBA) using gold nanoparticles as the SERS substrate and SCN^- as a vibrational Stark probe.[45]

Computational Methods

Classical MD Simulations. Classical molecular dynamics simulations were performed using GROMACS to characterize the interfacial distributions of PFOA, $K_2Cr_2O_7$, and their binary mixture at the air−water interface. Three liquid slab models were constructed: a PFOA-only system, a $K_2Cr_2O_7$-only system, and a binary PFOA−$K_2Cr_2O_7$ system, each containing two air−water interfaces. PFOA, water, and $K_2Cr_2O_7$ were described using the GAFF, TIP4P, and UFF-derived force fields, respectively.[46−48] After equilibration at 300 K under the NVT ensemble, each system was propagated under production conditions, and number-density profiles along the surface-normal

https://doi.org/10.1021/jacs.6c13880
J. Am. Chem. Soc. XXXX, XXX, XXX−XXX

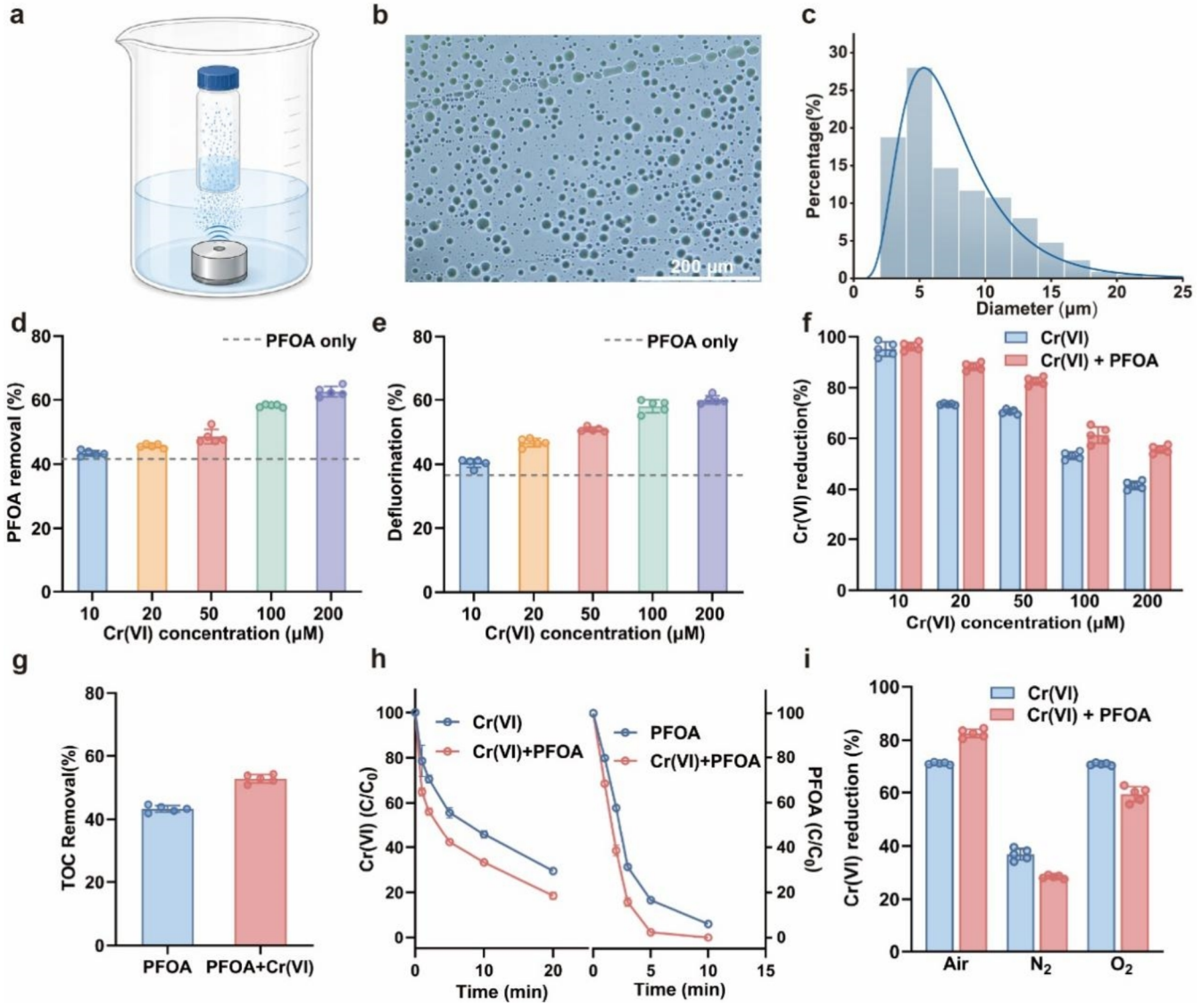

Figure 1. Cooperative removal of PFOA and Cr(VI) in aqueous microdroplets. (a) Schematic illustration of ultrasonic microdroplet generation. (b) Optical micrograph of the generated microdroplets. (c) Corresponding droplet-size distribution. (d) PFOA removal efficiency and (e) fluoride-release-based defluorination efficiency as functions of the initial Cr(VI) concentration; dashed lines indicate the corresponding PFOA-only baselines. (f) Cr(VI) reduction efficiency as a function of initial Cr(VI) concentration for Cr(VI) alone and the coexisting PFOA-Cr(VI) system. (g) Total organic carbon (TOC) removal for PFOA alone and the coexisting system. (h) Kinetic profiles of Cr(VI) reduction and PFOA removal in the single-contaminant and coexisting systems. (i) Effect of gas atmosphere (air, N_2, O_2) on Cr(VI) reduction in the single-contaminant and coexisting systems. Reaction conditions: $[PFOA]_{initial}$ = 5 mg·L^{-1}; $[Cr(VI)]_{initial}$ = 10−200 μM for (d−f), 50 μM for (g, h); reaction time, 2 min for (d, e) and 20 min for (f−i). For bar plots, individual points represent replicates and bars indicate the mean.

direction were calculated to evaluate interfacial enrichment and solute co-localization.

Ab Initio MD Simulations. Ab initio molecular dynamics simulations were performed using CP2K 2024.3 to compare the local solvation structure and electronic response of a representative PFOA−$K_2Cr_2O_7$ assembly under different hydration environments. The electronic structure was described at the PBE-D3 level using DZVP-MOLOPT-SR-GTH basis sets and GTH pseudopotentials.[49−51] Two solvation conditions were modeled: a fully solvated bulk model and a partially desolvated microdroplet model, each propagated in the NVT ensemble at 300 K.

Quantum Chemistry Calculations. Static electronic-structure calculations of the PFOA−$K_2Cr_2O_7$ assembly were carried out using ORCA 6.1.0 at the B3LYP-D3(BJ)/def2-TZVP level.[52,53] The B3LYP-D3(BJ) functional was employed consistently for comparative electronic-structure analysis of isolated PFOA and the PFOA-Cr(VI) assembly. Conceptual DFT descriptors, condensed Fukui functions, Mayer bond orders, and molecular electrostatic potentials were analyzed using Multiwfn.[54] To compare the kinetic accessibility of C−F bond activation, the activation barrier for a representative α-C−F bond cleavage step was further evaluated by periodic DFT calculations using VASP at the PBE-D3 level,[55] with the climbing-image nudged elastic band (CI-NEB) method used to locate the transition state.[56] Detailed model construction, force-field parameters, simulation time scales, convergence criteria, and post-processing procedures are provided in Text S8.

RESULTS AND DISCUSSION

Synergistic Enhancement of PFOA Degradation and Cr(VI) Reduction in the Coexisting Microdroplet System

In this study, aqueous microdroplets were produced by ultrasonic nebulization (Figure 1a).[57] The generated droplets exhibited a polydisperse size distribution in the micrometer

https://doi.org/10.1021/jacs.6c13880
J. Am. Chem. Soc. XXXX, XXX, XXX−XXX

range, with diameters mainly spanning approximately 2−20 μm (Figure 1b,c). Using this confined interfacial environment, we then examined whether the coexistence of PFOA and Cr(VI) could affect their respective transformation behaviors.[36]

Before analyzing the binary PFOA-Cr(VI) system, we established the single-solute behavior of PFOA and Cr(VI) under atomized microdroplet conditions. As shown in Figure S3, PFOA removal and Cr(VI) reduction were both below approximately 1% in the non-atomizing bulk-phase sonication controls but increased markedly upon atomization. These results establish the baseline for evaluating their coupled behavior and demonstrate that bulk-phase ultrasonic cavitation alone could not account for the observed reactivity. At an initial PFOA concentration of 5 mg·L^{-1} and a reaction time of 2 min, the parent-PFOA removal efficiency (Figure 1d) and fluoride-release-based defluorination efficiency (Figure 1e) were approximately 41.05% and 36.74%, respectively, in the PFOA-only system. As the initial Cr(VI) concentration increased from 10 to 200 μM, both efficiencies increased, reaching approximately 62.55% and 59.88%, respectively, at 200 μM Cr(VI). The parallel increase in PFOA depletion and F^- release suggests that Cr(VI) promotes not only the disappearance of the parent compound but also C−F bond cleavage. This interpretation is further supported by the TOC results, where removal increased from 43.27% for PFOA alone to 52.86% in the binary system, indicating a greater extent of transformation in the presence of Cr(VI) (Figure 1g). Consistent with this trend, quantitative headspace analysis showed that the CO_2 concentration increased from approximately 0.048% (v/v) in the air blank to 0.083% in the PFOA-only system and 0.091% in the PFOA-Cr(VI) system (Figure S5). The higher headspace CO_2 concentration in the binary system further supports enhanced PFOA oxidation and mineralization in the presence of Cr(VI), although the absolute increase in CO_2 remained small. Separately, to exclude equilibrium gas−liquid partitioning as an alternative explanation for the observed decrease in aqueous PFOA concentration, the distribution of PFOA between the aqueous phase and the headspace was estimated using Henry's law (Text S4). The calculated equilibrium gas-phase fraction was negligible under the experimental conditions, indicating that the decrease in aqueous PFOA concentration cannot be explained by equilibrium partitioning into the headspace. Cr(VI) reduction showed the opposite concentration dependence in the single system, decreasing from approximately 95.14% at 10 μM to approximately 39.49% at 200 μM as the initial Cr(VI) loading increased. Adding 5 mg·L^{-1} PFOA consistently improved Cr(VI) reduction, with the effect becoming more evident at higher Cr(VI) concentrations; at 200 μM Cr(VI), the reduction efficiency increased to approximately 55.68% (Figure 1f). Total Cr measurements further confirmed that chromium was largely retained in solution across the tested Cr(VI) concentration range in both the Cr(VI)-only and PFOA-Cr(VI) microdroplet systems (Figure S6). Thus, the observed decrease in Cr(VI) was not primarily attributable to chromium loss through precipitation, adsorption, or deposition on the reactor surface, but reflected a net change in chromium speciation. On this basis, the enhanced Cr(VI) depletion in the presence of PFOA can be interpreted as promoted net Cr(VI) reduction within the coexisting microdroplet system. These trends indicate that PFOA transformation and Cr(VI) reduction reinforce each other in microdroplets, rather than simply competing within the same reactive environment.

In the coexisting PFOA-Cr(VI) system, Cr(VI) reduction reached a given conversion within a shorter reaction time than in the corresponding single-solute system, and PFOA removal also proceeded more rapidly in the presence of Cr(VI) (Figure 1h). These results show that the difference between the single-solute and binary systems is not limited to end point efficiencies, but is also reflected in the temporal evolution of the reactions. The simultaneous enhancement of an oxidative pathway (PFOA defluorination) and a reductive pathway (Cr(VI) reduction) is consistent with the involvement of an interfacial redox network in the microdroplet environment, in which interfacial reactive species can simultaneously support oxidative and reductive transformations.[5,58] At this stage, however, the identities of the specific reactive intermediates remain tentative and require further mechanistic verification. To determine whether the enhanced Cr(VI) reduction arose solely from PFOA-derived products, sequential reagent-addition experiments were performed under matched ultrasonic nebulization times (Figure S7a,b and Text S5). PFOA pretreatment before Cr(VI) addition increased Cr(VI) reduction relative to the water-pretreatment control, confirming a contribution from PFOA-derived species. However, the greatest reduction was consistently observed when PFOA and Cr(VI) were introduced simultaneously, indicating that pre-generated products alone cannot explain the enhancement and highlighting the key promoting role of PFOA during Cr(VI) exposure. This conclusion was further supported by chain-length-dependent experiments using perfluorocarboxylic acids (PFCAs), with k_{obs} increasing with PFCA chain length (0.073−0.081 min^{-1}), compared with 0.061 min^{-1} for Cr(VI) alone (Figure S7c,d). The chain-length-dependent trend suggests that the molecular structure of the parent PFCAs influences Cr(VI) reduction, while the activity of shorter-chain PFCAs indicates that PFOA-derived transformation products may also contribute. Overall, the enhancement arises from the combined effects of PFOA and its transformation-derived species, with PFOA present during Cr(VI) exposure providing the strongest promotion.

Experiments conducted under different gas atmospheres provided additional mechanistic insight (Figure 1i). Under N_2 sparging, Cr(VI) reduction decreased substantially relative to ambient air, whereas an O_2-enriched atmosphere maintained or slightly enhanced the reduction efficiency. This trend is difficult to reconcile with a mechanism governed solely by direct interfacial electron transfer to Cr(VI), for which O_2 removal would be expected to increase the availability of reducing equivalents. Instead, the atmosphere dependence suggests that dissolved O_2 helps sustain oxygen-derived redox intermediates involved in Cr(VI) conversion. Recent studies have shown that dissolved O_2 redox underpins H_2O_2 and $^{\bullet}OH$ formation in aqueous microdroplets,[38] and that suppression of dissolved O_2 strongly inhibits H_2O_2 accumulation.[59] Together with the known reactivity between Cr(VI) and peroxide species, these observations support the involvement of an oxygen-coupled peroxide/ROS pathway in Cr(VI) transformation. The effect of PFOA on Cr(VI) reduction was atmosphere-dependent: PFOA enhanced Cr(VI) reduction under ambient air but decreased the reduction efficiency under N_2 and O_2 relative to the corresponding Cr(VI)-only controls. This mutual promotion also persisted across different water matrices (Figure S8). In each case, the coexisting PFOA-Cr(VI) system outperformed the corresponding single-contaminant controls and bulk-phase counterparts under microdroplet conditions. These results demonstrate that the synergistic interaction in the PFOA-

https://doi.org/10.1021/jacs.6c13880
J. Am. Chem. Soc. XXXX, XXX, XXX−XXX

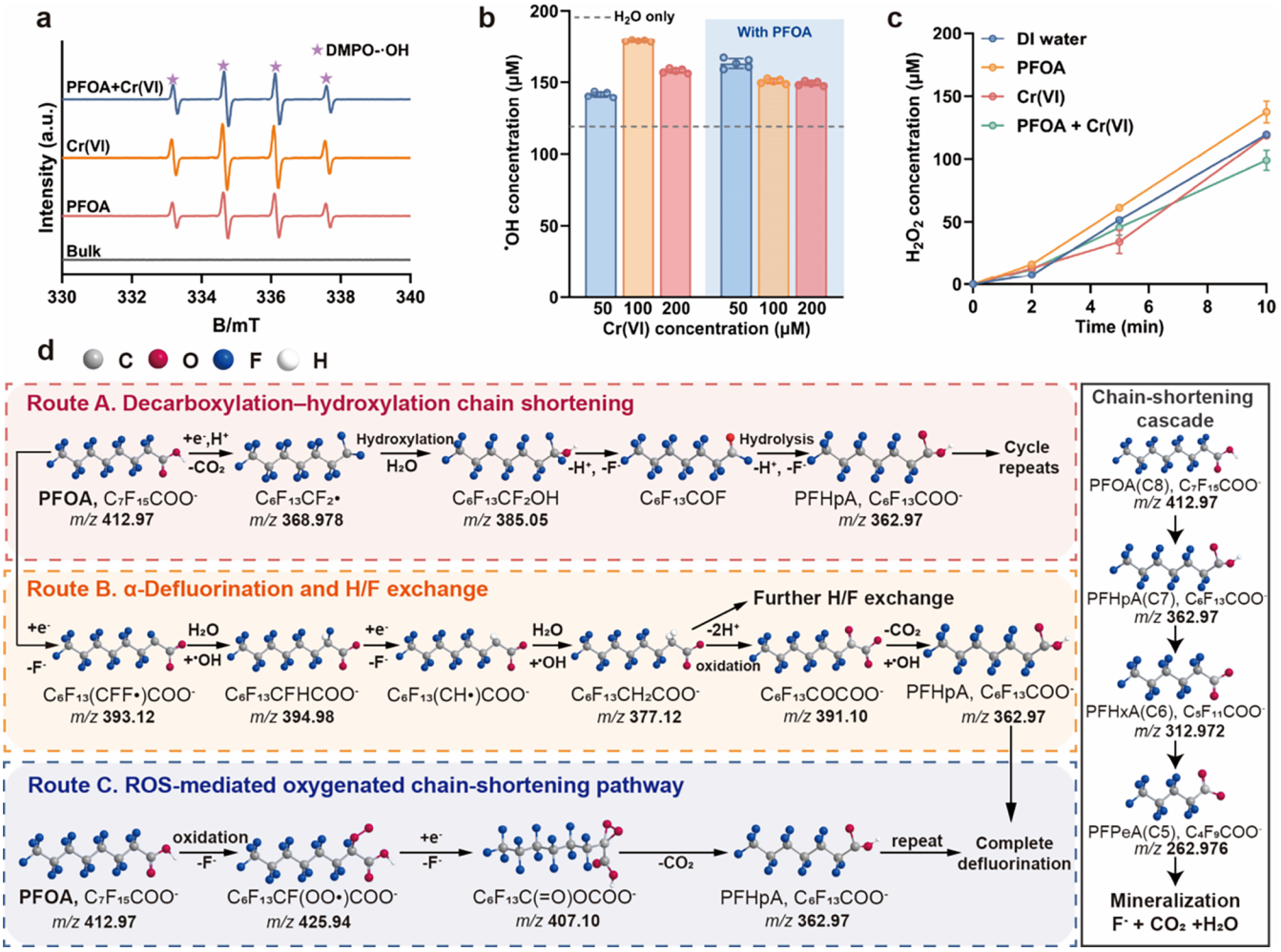

Figure 2. Reactive oxygen species generation and proposed PFOA degradation pathways in aqueous microdroplets. (a) Electron paramagnetic resonance (EPR) spectra recorded with DMPO as the spin trap for the PFOA, Cr(VI), and coexisting PFOA-Cr(VI) microdroplet systems, together with the bulk control without microdroplet generation. (b) $^{\bullet}$OH concentration as a function of Cr(VI) concentration in the absence and presence of PFOA; dashed line denotes the H_2O-only baseline. (c) H_2O_2 accumulation over reaction time for deionized water, PFOA, Cr(VI), and the coexisting system. (d) Proposed PFOA degradation pathways assigned from detected mass-to-charge ratios: Route A, decarboxylation/hydroxylation-mediated chain shortening; Route B, α-defluorination with H/F exchange; and Route C, ROS-mediated oxygenated chain shortening. Atom color code: C, gray; O, red; F, blue; H, white. Reaction conditions: $[PFOA]_{initial}$ = 5 mg·L^{-1}; $[Cr(VI)]_{initial}$ = 50−200 μM for (b); reaction time, 10 min for (b).

Cr(VI) system remains operative in complex aqueous environments, suggesting that microdroplet-based interfacial redox coupling may provide a promising strategy for treating multicomponent wastewaters containing both fluorinated organics and redox-active metals.

Interfacial ROS in the Synergistic Transformation

To clarify whether the enhanced PFOA defluorination originated from Cr(VI)-specific redox chemistry rather than nonspecific salt or reduced-chromium effects, two control electrolytes were examined under identical microdroplet conditions. K_2SO_4 (5−300 μM), spanning the relevant ionic-strength range, produced no enhancement in PFOA defluorination, whereas Cr(III) sulfate (10−200 μM), tested as a proxy for in situ-formed reduced chromium, caused only a weak concentration-dependent inhibition of F^- release rather than promotion (Figures S9 and S10). These results exclude electrolyte and reduced-chromium effects as the origin of the cooperative enhancement, consistent with a Cr(VI)-driven interfacial redox pathway at the microdroplet air−water interface.

Electron paramagnetic resonance (EPR) spin-trapping experiments were systematically performed to identify the ROS generated in microdroplets containing PFOA, Cr(VI), and their coexisting system. As shown in Figure 2a, $^{\bullet}$OH was detected in all three microdroplet systems. The signal intensity was markedly stronger in the Cr(VI)-containing systems than in the PFOA-only system, indicating that Cr(VI) promoted $^{\bullet}$OH generation at the microdroplet interface. Notably, the coexisting PFOA-Cr(VI) system retained a strong DMPO-$^{\bullet}$OH signal, although the intensity was slightly lower than that observed in the Cr(VI)-only system. This pattern suggests that PFOA did not abolish Cr(VI)-promoted $^{\bullet}$OH formation but may consume part of the generated $^{\bullet}$OH during interfacial transformation. This interpretation is further examined by the quantitative $^{\bullet}$OH and H_2O_2 data discussed below. Atmosphere-controlled EPR experiments provided further evidence for the oxygen-dependent pathway of $^{\bullet}$OH formation (Figure S11). The DMPO-$^{\bullet}$OH signal was dramatically enhanced under O_2 saturation and nearly abolished under N_2 purging, supporting an important role of dissolved O_2, or oxygen-derived intermediates, in the formation of DMPO-trappable $^{\bullet}$OH-related signals. This atmosphere

https://doi.org/10.1021/jacs.6c13880
J. Am. Chem. Soc. XXXX, XXX, XXX−XXX

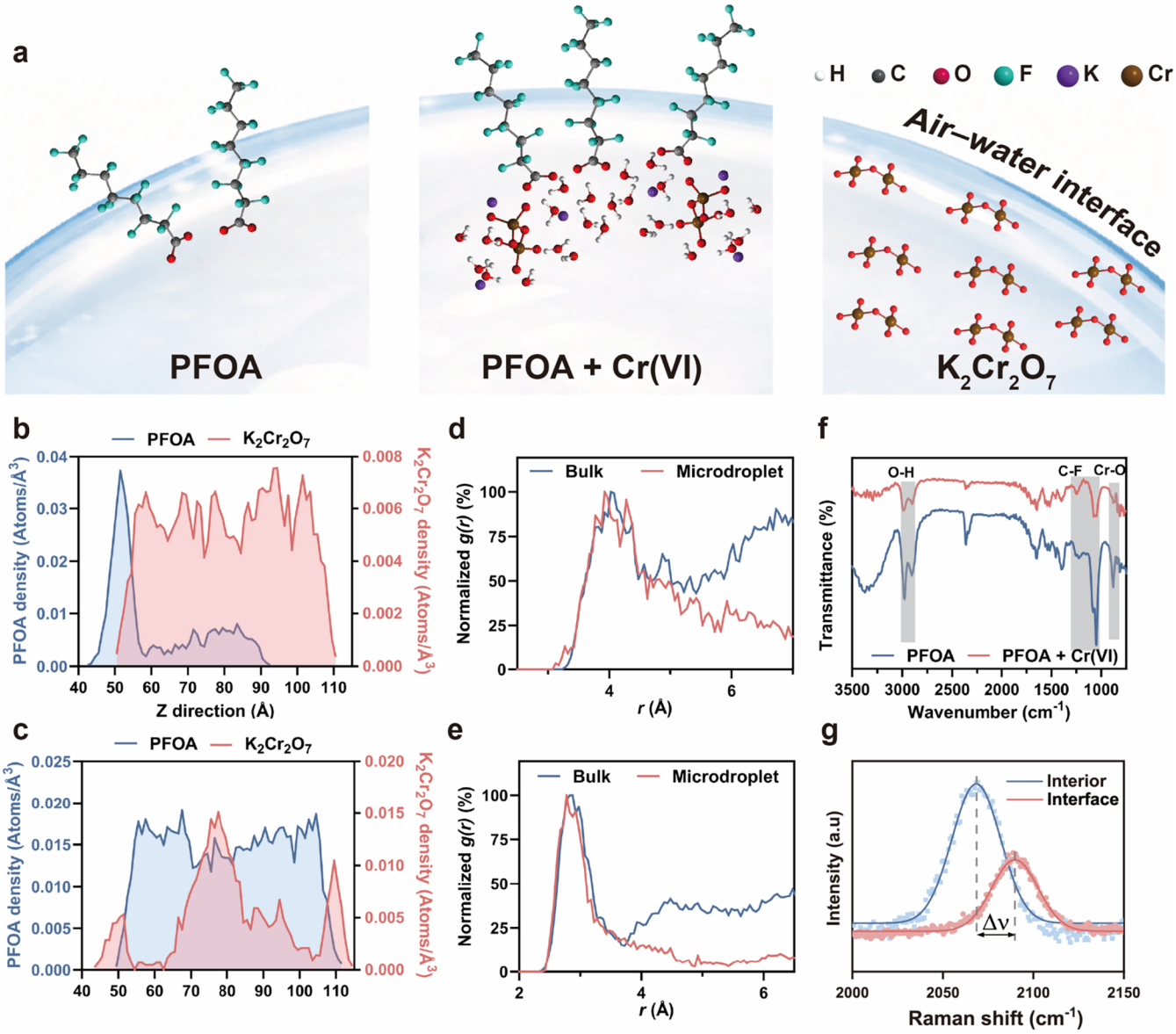

Figure 3. Interfacial co-enrichment and persistent association of PFOA and Cr(VI) at the microdroplet air–water interface. (a) Schematic representations of the interfacial distributions of PFOA-only, coexisting PFOA-$K_2Cr_2O_7$, and $K_2Cr_2O_7$-only systems. Classical-MD number-density profiles along the surface normal for (b) the single-solute and (c) the binary PFOA-$K_2Cr_2O_7$ systems. Peak-normalized AIMD radial distribution functions for (d) O–Cr and (e) O–K in the bulk and microdroplet models. (f) In situ ATR-FTIR spectra of PFOA and PFOA-$K_2Cr_2O_7$ systems. (g) Surface-enhanced Raman spectra of the SCN^- Stark probe in the droplet interior and at the air–water interface.

dependence is consistent with recent reports that dissolved O_2 contributes to H_2O_2 and $^{\bullet}OH$ generation in aqueous microdroplets, while the detailed elementary steps of oxygen activation may involve multiple short-lived intermediates.[39]

Quantitative $^{\bullet}OH$ measurements revealed a non-monotonic dependence on Cr(VI) concentration in the absence of PFOA, peaking at 100 μM before declining at 200 μM (Figure 2b), consistent with Cr-mediated Fenton-like chemistry at the microdroplet air–water interface.[13,38] Upon PFOA addition, $^{\bullet}OH$ concentrations remained above the DI water baseline at all Cr(VI) levels, but were lower than those in the corresponding Cr(VI) system at 100 and 200 μM Cr(VI). This attenuation supports partial $^{\bullet}OH$ consumption during PFOA transformation, while the sustained signal indicates continued Cr(VI)-promoted $^{\bullet}OH$ generation. Meanwhile, the k_{obs} values converged to a narrow range (0.194–0.205 min^{-1}, Table S1), close to that of the PFOA-only system (0.214 min^{-1}), suggesting that interfacially enriched PFOA moderates the Cr(VI)-driven increase in radical availability rather than abolishing it. Time-resolved profiles further confirmed continuous $^{\bullet}OH$ accumulation over 10 min, with the PFOA-Cr(VI) groups consistently exceeding the PFOA-only baseline (Figure S12). Together, these results suggest a dynamic balance between Cr(VI)-enhanced $^{\bullet}OH$ generation and PFOA-mediated radical consumption at the microdroplet interface, sustaining radical availability for the coupled transformation of PFOA and Cr(VI).

The temporal evolution of H_2O_2 was monitored to assess peroxide formation and its modulation by Cr species in microdroplets (Figure 2c). H_2O_2 accumulated over 10 min in all systems. Although these measurements do not reveal its molecular origin, they are consistent with electrochemical evidence of H_2O_2 formation in aqueous microdroplets.[43]

https://doi.org/10.1021/jacs.6c13880
J. Am. Chem. Soc. XXXX, XXX, XXX–XXX

Together with the atmosphere-dependent EPR results and previous reports on dissolved-O_2-derived peroxide and $^{\bullet}$OH-related intermediates,[38,59] these data support the involvement of an oxygen-coupled peroxide/ROS pathway. H_2O_2 accumulation was highest in the PFOA-only system but decreased markedly in the presence of Cr(VI), whereas DMPO-trapped $^{\bullet}$OH-related EPR signals increased. These opposing trends suggest that Cr species promote peroxide turnover. One plausible pathway is that lower-valent Cr intermediates formed during Cr(VI) reduction react with H_2O_2, thereby accelerating peroxide consumption and contributing to the formation of $^{\bullet}$OH-related oxidizing species.[20] The combined H_2O_2 and EPR responses are consistent with Cr-mediated peroxide activation during concurrent Cr(VI) reduction and PFOA oxidation at the microdroplet interface.

To elucidate the degradation pathways of PFOA in the microdroplet system, HPLC-MS analysis was performed to identify the transformation intermediates and products formed in both the PFOA-only and PFOA-Cr(VI) systems. Notably, the degradation intermediates detected in the PFOA-Cr(VI) system largely overlapped with those observed in the PFOA-only system (Figure 2d), suggesting that the presence of Cr(VI) does not substantially alter the primary degradation network of PFOA, but rather enhances the turnover of transformation channels that are intrinsically accessible at the microdroplet interface. On the basis of the detected intermediates, PFOA transformation proceeds through three parallel pathways: stepwise decarboxylation−hydroxylation chain shortening,[16] α-defluorination coupled with H/F exchange,[17,60] and a ROS-mediated oxygenated chain-shortening pathway.[58,61] The coexistence of short-chain PFCAs, defluorinated/hydrogenated products, and oxygen-containing intermediates indicates a dual-redox interfacial environment. Here, oxygen-derived radical chemistry and reductive electron-transfer processes operate concurrently on interfacially enriched PFOA.[62] In this system, Cr(VI) does not appear to create a new PFOA degradation network, but functions primarily as a kinetic and redox modulator. By accepting interfacial electrons and promoting H_2O_2 activation to $^{\bullet}$OH through Cr redox cycling, it increases the steady-state flux of reactive intermediates and thereby enhances both PFOA defluorination and Cr(VI) reduction. The detailed reaction sequences, intermediate assignments, and mass spectrometric evidence for each pathway are provided in the Supporting Information (Figure S13).

Collectively, these results demonstrate that the microdroplet air−water interface provides a redox-active environment capable of sustaining both oxidative and reductive chemistry. This interfacial redox network enables PFOA degradation and Cr(VI) reduction to proceed concurrently and cooperatively, providing a mechanistic basis for their mutually promoted transformation in microdroplets.

Molecular-Level Insights into Interfacial Co-Enrichment and Complex Formation

To clarify the structural origin of the experimentally observed synergistic PFOA-Cr(VI) interaction, we examined how the two species organize at the air−water interface of the microdroplet. Two complementary simulations operating at different length and time scales were employed: classical MD to resolve the ensemble-level spatial organization of multiple PFOA and $K_2Cr_2O_7$ units in slab models of the air−water interface, and ab initio molecular dynamics (AIMD) to probe the local electronic and structural stability of a representative PFOA-Cr(VI) assembly (modeled as PFOA-$K_2Cr_2O_7$) under both bulk-solvated and partially desolvated interfacial conditions. This multiscale framework is well suited to microdroplet systems, where collective interfacial organization and local site-specific reactivity must be addressed simultaneously.

To characterize the interfacial distribution of PFOA and Cr(VI), classical MD simulations were performed on three independent slab systems: a PFOA-only system, a $K_2Cr_2O_7$-only system, and their binary mixture (Figure S14). In the single-solute simulations, PFOA migrated spontaneously from the aqueous subphase to the air−water interface within the equilibration period, generating pronounced density maxima at both interfacial boundaries (Figure 3b). The resulting steady-state interfacial population substantially exceeded that in the bulk aqueous subphase, reflecting the thermodynamic preference of the perfluorinated tail for the low-polarity vapor side of the interface and the electrostatic anchoring of the carboxylate headgroup within the aqueous phase.[63] This surface-active behavior is consistent with prior molecular dynamics studies of PFOA and structurally related perfluoroalkyl surfactants at fluid−fluid interfaces.[64] In the $K_2Cr_2O_7$-only system, by contrast, $Cr_2O_7^{2-}$ and K^+ remained distributed uniformly throughout the aqueous phase, showing no statistically significant accumulation at either interface, in accord with the strong hydration free energy of dichromate and the absence of any hydrophobic driving force for interfacial adsorption.[65,66]

A qualitatively distinct spatial organization emerged in the binary system. Beyond the anticipated interfacial enrichment of PFOA, both $Cr_2O_7^{2-}$ and K^+ developed a marked population near the PFOA-rich interfacial layer rather than remaining dispersed in the aqueous subphase (Figure 3c). The probability of finding $K^+/Cr_2O_7^{2-}$ in the interfacial region was substantially higher in the binary system than in the corresponding single-solute simulation, indicating that adsorbed PFOA facilitates redistribution of the $K_2Cr_2O_7$-derived ions toward the interface. This co-enrichment is most plausibly attributed to electrostatic association between the PFOA headgroup and its counterions, together with local cation-mediated screening that lowers the energetic penalty for $Cr_2O_7^{2-}$ residing in the same interfacial region. This interpretation is consistent with the broader framework of charged-amphiphile interfacial organization, in which favorable fluorocarbon-chain interactions and unfavorable Coulomb interactions can nearly compensate, making counterion distribution and ionic screening key determinants of interfacial structure.[67] Recent MD studies further reveal that PFOA in particular tends to form in-plane clusters with its counterions at the air−water interface, owing to the strong localization of negative charge on the carboxylate oxygens.[3] The resulting spatial co-localization of an oxidizable organic substrate and a reducible inorganic oxidant within a shared interfacial domain provides the structural foundation for the coupled redox transformations observed experimentally.

Spatial co-localization, however, does not by itself imply that PFOA and Cr(VI) form an electronically coupled assembly under the partially desolvated conditions of the microdroplet interface. To assess whether such co-localization yields a persistent assembly with a distinct electronic structure, we combined AIMD simulations of a representative PFOA-Cr(VI) assembly (modeled as PFOA-$K_2Cr_2O_7$) in a fully solvated bulk model and in a partially desolvated microdroplet model (Figure S15) with in situ ATR-FTIR and vibrational Stark-effect measurements. Peak-normalized radial distribution functions reveal that the first hydration environment around the Cr(VI)

https://doi.org/10.1021/jacs.6c13880
J. Am. Chem. Soc. XXXX, XXX, XXX−XXX

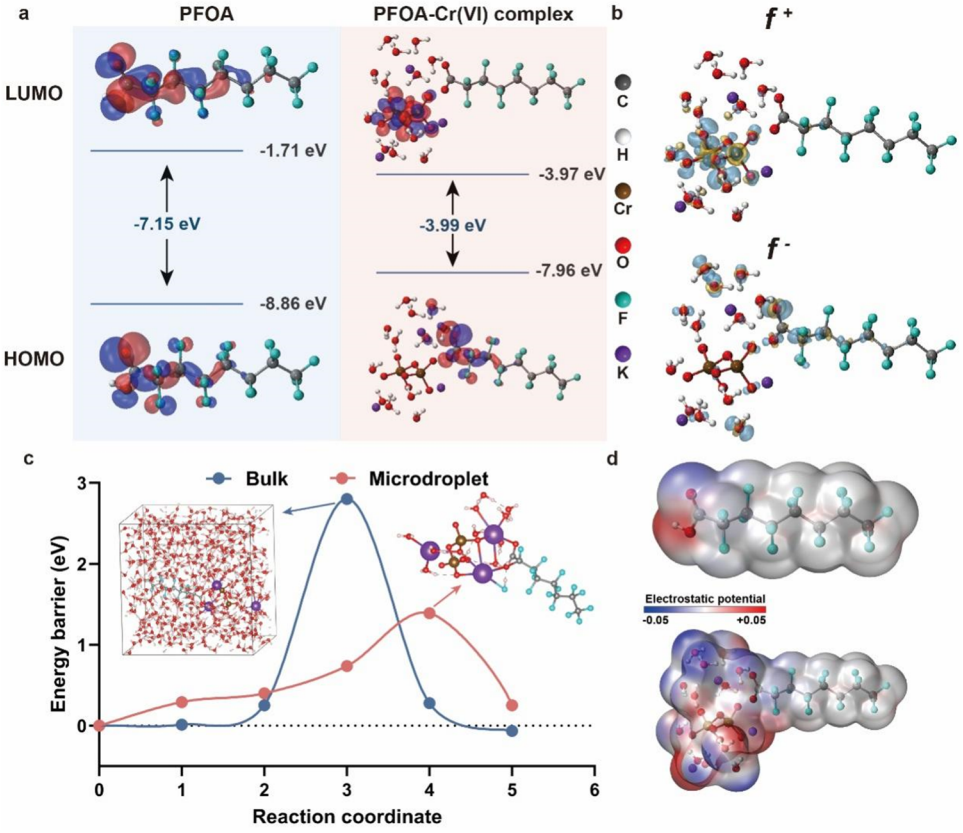

Figure 4. Electronic structure and interfacial C−F bond activation of the PFOA-Cr(VI) system from DFT calculations. (a) Frontier molecular orbitals (HOMO and LUMO) and relative HOMO−LUMO gaps for isolated PFOA and the PFOA-Cr(VI) assembly calculated at the same theoretical level; orbital energies are provided for qualitative comparison. (b) Condensed Fukui function isosurfaces for the PFOA-Cr(VI) assembly: f^+ (electron-accepting/nucleophilic-attack susceptibility) and f^- (electron-donating/electrophilic-attack susceptibility). (c) Energy barrier along the representative α-C−F bond cleavage reaction coordinate in the bulk model and the microdroplet model, obtained by CI-NEB; insets show representative configurations of the two environments. (d) Electrostatic potential (ESP) mapped onto the molecular surface of PFOA (top) and the PFOA-Cr(VI) assembly (bottom); color scale from −0.05 to +0.05 a.u. Atom color code: C, gray; H, white; O, red; F, cyan; Cr, brown; K, purple.

oxyanion is largely preserved in both environments, while the outer coordination shells are markedly attenuated in the microdroplet model, consistent with partial desolvation at the droplet surface (Figure 3d,e). These observations indicate that the air−water interface induces partial desolvation of the assembly without disrupting its local coordination geometry, producing instead a compressed and reorganized hydration environment.[68] These results suggest that interfacially co-localized PFOA and $K_2Cr_2O_7$-derived ions remain locally associated over the AIMD simulation time scale. Partial desolvation attenuates the outer hydration shells without substantially disrupting the first coordination environment.

Complementary in situ ATR-FTIR spectroscopy was used to probe the vibrational response of PFOA microdroplets upon Cr(VI) addition (Figure 3f). Relative to PFOA alone, the PFOA-Cr(VI) system showed more pronounced absorption in the C−F stretching region near 1200 cm^{-1} without an obvious peak shift, suggesting a modified local environment of the perfluorinated chain rather than substantial disruption of the C−F framework. The broadened O−H band near 3000 cm^{-1} further indicates reorganization of the hydrogen-bonding network around the PFOA headgroup. Meanwhile, the enhanced Cr−O feature near 880 cm^{-1} supports the presence of Cr(VI) oxyanions within the ATR sampling region. Although ATR-FTIR probes the vibrational response within the ATR sampling region rather than exclusively the outermost air−water interface, these vibrational changes corroborate that Cr(VI) addition modifies the local solvation and bonding environment of PFOA-containing microdroplets, consistent with the interfacial organization suggested by the MD simulations. To further verify that these spectral changes were not specifically induced by ultrasonic aerosolization, ATR-FTIR measurements were additionally performed using non-sonicated spray-generated aqueous microdroplets. Similar spectral variations between PFOA and PFOA-Cr(VI) systems were observed (Figure S16), supporting the intrinsic interfacial association between PFOA and Cr(VI) in aqueous microdroplets. To experimentally probe the local electrostatic environment of this coexisting system in microdroplets, we used SCN^- as a vibrational Stark-effect probe in surface-enhanced Raman measurements.[69,70] As shown in Figure 3g, the $\nu(C{\equiv}N)$ band shifted from 2068 cm^{-1} in the droplet interior to 2089 cm^{-1} at the air−water interface, corresponding to an electric field strength of 5.8×10^7 V cm^{-1}. This value is on the same order of magnitude as those reported for aqueous microdroplet surfaces and is consistent with the presence of a strong interfacial electric field in the PFOA-Cr(VI) coexisting system.[35] Taken together, the MD density profiles, AIMD structural analysis, and Stark-probe measurements indicate that the microdroplet interface serves not only as a site of solute co-enrichment but also as an electrostatically distinct reaction microenvironment, thereby

https://doi.org/10.1021/jacs.6c13880
J. Am. Chem. Soc. XXXX, XXX, XXX−XXX

providing a structural and electrostatic basis for the electronic polarization and C−F bond activation examined below.

Electronic Structure and Interfacial C−F Bond Activation in the PFOA-Cr(VI) System

Having established the interfacial co-enrichment and persistent association of PFOA and Cr(VI), we next sought to determine how the air−water interface electronically organizes PFOA oxidative defluorination and Cr(VI) reduction within a shared reaction microenvironment. This question is central to the cooperative transformation observed experimentally: PFOA must be activated toward C−F bond cleavage, while Cr(VI) must remain positioned as a proximal multi-electron acceptor. We therefore combined frontier-orbital analysis, conceptual DFT descriptors, electrostatic-potential mapping, and climbing-image nudged elastic band calculations to clarify how Cr(VI) association and microdroplet confinement jointly reshape the electronic and kinetic landscape of the coupled redox process.

As a molecular reference for the PFOA-only system, free PFOA displays a large HOMO−LUMO gap of 7.153 eV and a negative vertical electron affinity, reflecting the intrinsic electronic inertness of perfluorinated carboxylates (Figure 4a).[1,4] It should be noted that B3LYP may not provide quantitatively accurate absolute frontier orbital energies due to its limited long-range exchange correction.[71−73] Therefore, the calculated HOMO−LUMO values are interpreted here as relative descriptors of electronic structure evolution upon Cr(VI) association. Association with Cr(VI) fundamentally changes this picture by converting the otherwise inert PFOA terminus into part of a polarized donor−acceptor contact zone (Figure S17). As shown in Figure 4a, the HOMO−LUMO gap decreases from 7.153 to 3.993 eV upon formation of the PFOA-Cr(VI) assembly, indicating substantially enhanced electronic susceptibility. Consistent with this, the global electrophilicity index ω more than doubles from 1.275 eV (PFOA) to 2.642 eV (PFOA-Cr(VI) assembly) at the same level of theory (Table S2), confirming the greater capacity of the assembly to accept electron density. The Fukui-function distributions further reveal how this enhanced electronic susceptibility is spatially organized within the PFOA-Cr(VI) assembly (Figure 4b). Pronounced f^+ contributions emerge around the Cr center and coordinated dichromate oxygens, identifying the Cr(VI) moiety as the dominant electron-accepting domain. In contrast, the headgroup-proximal region of PFOA remains the most chemically susceptible site for activation. The corresponding f^- distribution localizes on a different subset of dichromate oxygens, producing a spatial separation between electron-accepting and electron-donating regions across the Cr−O−PFOA contact region. Thus, Cr(VI) does not merely act as an external oxidant in solution; it becomes electronically integrated with PFOA at the interface, creating a contact zone in which electron release from PFOA oxidative defluorination can be coupled to Cr(VI) reduction.

These results point to the α-C−F bond next to the carboxylate group as a likely initiation site for PFOA activation. The electrostatic potential map of free PFOA shows pronounced headgroup polarization, with electron-rich carboxylate oxygens and an electron-deficient region near the carboxylate carbon (Figure 4d). Upon association with Cr(VI), this polarized region extends toward the dichromate moiety, placing the α-C−F bond in a strongly perturbed electrostatic environment. This configuration favors activation near the carboxylate terminus over the more remote C−F bonds along the perfluorinated chain. This feature indicates enhanced susceptibility of the headgroup-proximal C−F bond to interfacial polarization and electron-coupled activation (Figure 4d). This assignment is also chemically reasonable because the α-C−F bond experiences the strongest inductive influence from the carboxylate group and remains more sterically accessible than C−F bonds along the distal perfluorinated chain.[74] Consistently, Mayer bond-order analysis identifies the headgroup-proximal C−F bond (bond order 0.916) as the weakest C−F bond in PFOA, well below the average value of 1.07 for the remaining C−F bonds, supporting its preferential activation (Table S3). Therefore, the Cr(VI)-associated headgroup region represents a chemically plausible initiation site for oxidative defluorination. This conclusion is consistent with the α-defluorinated and chain-shortened intermediates detected by mass spectrometry, supporting a mechanism in which C−F activation can initiate near the carboxylate terminus and proceed in parallel with internal-chain oxidation and chain-shortening pathways.[17,60]

We next asked whether this electronically preferred activation pathway is kinetically enabled by interfacial confinement. Reaction-energy profiles for the representative α-C−F bond cleavage step show that the activation barrier decreases from 2.802 eV in the bulk model to 1.390 eV in the microdroplet model, corresponding to a barrier reduction of 1.412 eV (Figure 4c). Thus, the air−water interface not only polarizes the headgroup-proximal C−F bond but also lowers the kinetic threshold for initiating PFOA oxidative defluorination. Several interfacial features are likely to contribute to this kinetic advantage. Partial desolvation at the interface lowers the solvent-reorganization energy required to reach the transition state. In addition, the strong interfacial electric field polarizes the C−F bond and stabilizes charge-separated transition states.[27,75] This field-assisted activation picture is consistent with recent experimental and computational evidence from contact-electrified polymer-water interfaces, where strong interfacial electrostatic fields polarize PFOA and markedly lower the activation barrier for $O_2^{\bullet-}$-initiated defluorination at the α-CF_2 site.[76] AIMD-derived hydrogen-bond analysis further supports a more labile interfacial solvation environment: although O−H···O hydrogen bonds dominate in both models, their average maximum continuous lifetime decreases from 279.0 fs in the bulk-like model to 227.3 fs in the microdroplet model, and the survival probability at 500 fs decreases from approximately 0.20 to 0.06 (Figure S18). The absence of a long-lived decay plateau at the interface indicates a dynamically reconfigurable hydrogen-bond network that can more readily accommodate evolving reactive configurations. Although the CI-NEB pathway models a single elementary step rather than the full degradation network, it captures a clear kinetic distinction between bulk water and the microdroplet interface.

Taken together, these results indicate that the microdroplet interface does not simply accelerate C−F bond cleavage in isolation. Instead, it organizes PFOA oxidative defluorination and Cr(VI) reduction into a shared, electronically polarized redox microenvironment. Cr(VI) association narrows the frontier-orbital gap, redistributes local Fukui reactivity, and establishes a proximal multi-electron accepting domain adjacent to the PFOA headgroup. Concurrently, the partially desolvated and electrostatically polarized air−water interface lowers the barrier for the headgroup-proximal C−F activation step, enabling electron release from PFOA degradation to be electronically coupled to Cr(VI) reduction within the same contact zone. This combination of interfacial co-localization, donor−acceptor electronic polarization, and kinetic barrier

https://doi.org/10.1021/jacs.6c13880
J. Am. Chem. Soc. XXXX, XXX, XXX−XXX

lowering provides a molecular-level rationale for the experimentally observed mutual promotion of PFOA defluorination and Cr(VI) reduction in microdroplets.

Integrated Mechanism of Electron-Coupled Redox Chemistry at the Microdroplet Interface

Based on the foregoing experimental and computational evidence, we propose an integrated mechanism for the coupled transformation of PFOA and Cr(VI) at the microdroplet air−water interface. In this model, the amphiphilic structure of PFOA drives its spontaneous enrichment at the droplet surface,[58] with the perfluorinated chain oriented toward the low-polarity interfacial region and the carboxylate headgroup retained on the aqueous side. This PFOA-rich interfacial layer reorganizes the local ionic environment and promotes the co-enrichment of K^+ and Cr(VI) oxyanions through PFOA headgroup−K^+ association and cation-mediated electrostatic screening, thereby confining an oxidizable perfluorinated substrate and a reducible inorganic oxyanion within the same reactive interfacial domain.

Within this co-enriched interfacial region, charge separation and the strong local electric field support oxygen-coupled redox chemistry, giving rise to a network of reactive intermediates that includes $O_2^{\bullet-}$/$^{\bullet}$OOH, H_2O_2, and $^{\bullet}$OH-related signals.[38] Cr(VI) is proposed to act as a proximal electron acceptor and, through subsequent Cr redox chemistry, promotes H_2O_2 activation to $^{\bullet}$OH,[20] thereby increasing the local radical flux available for PFOA transformation. However, the product distributions indicate that Cr(VI) does not redirect PFOA degradation into an entirely new pathway. Instead, it accelerates degradation pathways that are already accessible at the microdroplet interface,[5] including chain shortening, headgroup-proximal C−F activation, and localized oxidative modification.

This coupled behavior is further amplified by the unique solvation environment of the microdroplet interface. Partial desolvation, a more reconfigurable hydrogen-bond network, and interfacial electrostatic polarization stabilize a persistent PFOA-Cr(VI) assembly and lower the kinetic barrier for C−F bond cleavage.[27,68] Thus, PFOA degradation and Cr(VI) reduction are not independent parallel reactions, but are coupled through interfacial redox coupling.[36] The microdroplet interface therefore acts as an active redox-organizing medium that preconcentrates reactants, sustains oxygen-derived radical chemistry, and integrates organic defluorination with inorganic reduction within a confined reaction microenvironment.

CONCLUSIONS

This study shows that the spatial organization of redox demand at the air−water interface governs the coupling of PFAS C−F bond activation with multi-electron metal reduction under ambient conditions. In aqueous microdroplets, electrostatic polarization co-enriches PFOA and Cr(VI) within a confined interfacial domain, promoting Cr-associated reactive-species generation and concurrent PFOA transformation. This coupling increases PFOA defluorination by approximately 63% and Cr(VI) reduction by approximately 41%. The results support a mechanism involving interfacial co-localization, oxygen-coupled ROS generation, Cr-mediated H_2O_2 activation and microdroplet-specific solvation. Partial desolvation and dynamic reorganization of the hydrogen-bond network further lower the barrier to α−C−F cleavage. Together, these effects create a shared interfacial redox environment that facilitates both organofluorine defluorination and Cr(VI) reduction. These findings position aqueous microdroplets as interfacial reactors capable of coordinating mechanistically distinct contaminant transformations. The present study focuses on the mechanistic behavior of PFOA and Cr(VI) in an ultrasonically generated microdroplet system. Because ultrasonic atomization requires external energy, its energy efficiency and scalability should be further evaluated when considering engineered treatment applications. Further work combining ultrafast transient absorption and vibrational sum-frequency generation spectroscopy with enhanced-sampling AIMD and QM/MM simulations could resolve the underlying electron- and radical-transfer events. Validation in complex industrial matrices, including electroplating effluents and PFAS-contaminated groundwater, will be essential to determine the practical viability of this approach for the simultaneous remediation of PFAS and redox-active metals.

ASSOCIATED CONTENT

Supporting Information

The Supporting Information is available free of charge at https://pubs.acs.org/doi/10.1021/jacs.6c13880.

Experimental and computational methods; characterization, control and kinetic experiments, reactive-species and transformation-product analyses, gas−liquid partitioning calculations, and simulation results (PDF)

AUTHOR INFORMATION

Corresponding Authors

Yuliang Li − *State Key Laboratory of Pollution Control and Resource Reuse, School of Environment, Nanjing University, Nanjing 210023 Jiangsu Province, China*; Email: leo@nju.edu.cn

Dongmei Zhou − *State Key Laboratory of Pollution Control and Resource Reuse, School of Environment, Nanjing University, Nanjing 210023 Jiangsu Province, China*; orcid.org/0000-0002-7917-7954; Email: dmzhou@nju.edu.cn

Authors

Xiaoke Ma − *State Key Laboratory of Pollution Control and Resource Reuse, School of Environment, Nanjing University, Nanjing 210023 Jiangsu Province, China*

Ronghao Wu − *State Key Laboratory of Pollution Control and Resource Reuse, School of Environment, Nanjing University, Nanjing 210023 Jiangsu Province, China*; orcid.org/0009-0003-1330-1363

Min Wang − *State Key Laboratory of Environmental Chemistry and Ecotoxicology, Research Center for Eco-Environmental Sciences, Chinese Academy of Sciences, Beijing 100085, China*

Jinsong Liu − *State Key Laboratory of Pollution Control and Resource Reuse, School of Environment, Nanjing University, Nanjing 210023 Jiangsu Province, China*

Longgang Chu − *State Key Laboratory of Pollution Control and Resource Reuse, School of Environment, Nanjing University, Nanjing 210023 Jiangsu Province, China*; orcid.org/0009-0003-3125-8039

Xiaolei Wang − *State Key Laboratory of Pollution Control and Resource Reuse, School of Environment, Nanjing University, Nanjing 210023 Jiangsu Province, China*; orcid.org/0000-0002-6535-0744

Complete contact information is available at:

https://pubs.acs.org/10.1021/jacs.6c13880

Notes

The authors declare no competing financial interest.

■ ACKNOWLEDGMENTS

This is financially supported by the National Natural Science Foundation of China (22176091 and 42130707) and the China Postdoctoral Science Foundation (2025M781184).

■ REFERENCES

(1) Evich, M. G.; Davis, M. J. B.; McCord, J. P.; Acrey, B.; Awkerman, J. A.; Knappe, D. R. U.; Lindstrom, A. B.; Speth, T. F.; Tebes-Stevens, C.; Strynar, M. J.; Wang, Z.; Weber, E. J.; Henderson, W. M.; Washington, J. W. Per- and polyfluoroalkyl substances in the environment. *Science* **2022**, *375* (6580), No. eabg9065.

(2) Whitehead, H. D.; Venier, M.; Wu, Y.; Eastman, E.; Urbanik, S.; Diamond, M. L.; Shalin, A.; Schwartz-Narbonne, H.; Bruton, T. A.; Blum, A.; Wang, Z.; Green, M.; Tighe, M.; Wilkinson, J. T.; McGuinness, S.; Peaslee, G. F. Fluorinated compounds in North American cosmetics. *Environ. Sci. Technol. Lett.* **2021**, *8* (7), 538−544.

(3) Lemay, A. C.; Bourg, I. C. Interactions between per- and polyfluoroalkyl substances (PFAS) at the water−air interface. *Environ. Sci. Technol.* **2025**, *59* (4), 2201−2210.

(4) Sinha, S.; Chaturvedi, A.; Gautam, R. K.; Jiang, J. Molecular Cu electrocatalyst escalates ambient perfluorooctanoic acid degradation. *J. Am. Chem. Soc.* **2023**, *145* (50), 27390−27396.

(5) Xia, D.; Zhang, H.; Ju, Y.; Xie, H.; Su, L.; Ma, F.; Jiang, J.; Chen, J.; Francisco, J. S. Spontaneous degradation of the "forever chemicals" perfluoroalkyl and polyfluoroalkyl substances (PFASs) on water droplet surfaces. *J. Am. Chem. Soc.* **2024**, *146* (16), 11266−11271.

(6) Luo, S.; Xie, Z.; Xiong, X.; Bai, L.; Wang, H.; Wei, Z. Activating PFAS to unlock efficient defluorination. *Environ. Sci. Technol.* **2025**, *59* (39), 20910−20918.

(7) Jiang, X.; Zhou, Z.; Qin, Z.; Ou, T.; Zhang, Q.; Zhang, H.; Wu, X.; He, S.; Meng, B.; Ge, Y.; Huang, J.; Zhang, Y.; Peng, Z.; Yu, G.; Deng, S. Occurrence, transport, and full-scale adsorptive removal of PFAS in electroplating parks in China. *Environ. Sci. Technol.* **2024**, *58* (51), 22744−22754.

(8) Zhang, B.-X.; Meng, X.-Z.; Han, B.-C.; Zhao, Z.; He, Q.-W.; Ma, C.-D.; Zhu, Q.; Yang, J.; Qin, H.; Wang, Y. Elaborating PFAS characteristics for Chinese electroplating industry by target and nontarget analysis. *Water Res.* **2025**, *287*, No. 124405.

(9) Zhigalenok, Y.; Tazhibayeva, A.; Kokhmetova, S.; Starodubtseva, A.; Kan, T.; Isbergenova, D.; Malchik, F. Hexavalent chromium at the crossroads of science, environment and public health. *RSC Adv.* **2025**, *15* (27), 21439−21464.

(10) Tshangana, C. S.; Nhlengethwa, S. T.; Glass, S.; Denison, S.; Kuvarega, A. T.; Nkambule, T. T. I.; Mamba, B. B.; Alvarez, P. J. J.; Muleja, A. A. Technology status to treat PFAS-contaminated water and limiting factors for their effective full-scale application. *npj Clean Water* **2025**, *8* (1), No. 41.

(11) Liu, X.; Sau, A.; Green, A. R.; Popescu, M. V.; Pompetti, N. F.; Li, Y.; Zhao, Y.; Paton, R. S.; Damrauer, N. H.; Miyake, G. M. Photocatalytic C−F bond activation in small molecules and polyfluoroalkyl substances. *Nature* **2025**, *637* (8046), 601−607.

(12) Jiang, Z.; Liu, Y.; Lindh, C.; Pineda, D.; Carøe, T. K.; Catalán, J.; Ebbehøj, N. E.; Givelet, L.; Huusom, A. J.; Kines, P.; Krais, A. M.; Aimonen, K.; Lundh, T.; Loeschner, K.; Rastkhani, H.; Tondel, M.; Saber, A. T.; Vogel, U.; Broberg, K. Per- and polyfluoroalkyl substances exposure in hexavalent chromium exposed workers and the effects of exposure mixtures on oxidative stress and genomic instability. *Environ. Pollut.* **2025**, *387*, No. 127255.

(13) Yao, S.; Ma, J.; Ma, D.; Sillanpää, M. E. T.; Zhou, M.; Ye, Q.; Jin, H.; Zhang, K. Comprehensive evaluation and mechanistic comparison of Cr-catalyzed homogeneous fenton-like reactions for coexisting organics degradation. *Chem. Eng. J.* **2024**, *502*, No. 157918.

(14) Ding, W.; Tang, T.; Tan, X.; Huang, Y. Enhancing photocatalytic decarboxylation by frustrated lewis acid−base pairs for efficient degradation of perfluorooctanoic acid. *Environ. Sci. Technol.* **2025**, *59* (33), 17899−17908.

(15) Glass, S.; Kannan, H.; Bangala, J.; Chen, Y.; Metz, J.; Mowzoon-Mogharrabi, R.; Gao, G.; Meiyazhagan, A. K.; Wong, M. S.; Ajayan, P. M.; Senftle, T. P.; Alvarez, P. J. J. Iron doping of hBN enhances the photocatalytic oxidative defluorination of perfluorooctanoic acid. *ACS Appl. Mater. Interfaces* **2025**, *17* (15), 22803−22811.

(16) Trang, B.; Li, Y.; Xue, X.-S.; Ateia, M.; Houk, K. N.; Dichtel, W. R. Low-temperature mineralization of perfluorocarboxylic acids. *Science* **2022**, *377* (6608), 839−845.

(17) Biswas, S.; Yamijala, S. S. R. K. C.; Wong, B. M. Degradation of per- and polyfluoroalkyl substances with hydrated electrons: a new mechanism from first-principles calculations. *Environ. Sci. Technol.* **2022**, *56* (12), 8167−8175.

(18) Li, K.; You, W.; Wang, W.; Gong, K.; Liu, Y.; Wang, L.; Ge, Q.; Ruan, X.; Ao, J.; Ji, M.; Zhang, L. Significantly accelerated photochemical perfluorooctanoic acid decomposition at the air−water interface of microdroplets. *Environ. Sci. Technol.* **2023**, *57* (50), 21448−21458.

(19) Wang, K.; Li, H.; Liu, H.; Hou, C.; Zhou, Z.; Peng, S.; Chen, Z.; Lei, Z.; Wu, D. Mechanochemical-triggered confined coordination of iron-biomass composites for efficient Cr(VI) reduction under circum-neutral pH via accelerated electron extraction. *Adv. Sci.* **2025**, *12* (15), No. 2417368.

(20) Bokare, A. D.; Choi, W. Advanced oxidation process based on the Cr(III)/Cr(VI) redox cycle. *Environ. Sci. Technol.* **2011**, *45* (21), 9332−9338.

(21) Wang, X.; Tong, Y.; Zhu, C.; Zhu, F.; Fang, G.; Zhang, S.; Zhou, D. Efficient reduction of Cr(VI) under alkaline condition by alcohol radicals: performance, radical generation, and mechanisms. *Chem. Eng. J.* **2026**, *528*, No. 172514.

(22) Chen, X.; Xia, Y.; Yang, Y.; Xu, Y.; Jia, X.; N Zare, R.; Wang, F. Microdroplet-mediated multiphase cycling in a cloud of water drives chemoselective electrolysis. *J. Am. Chem. Soc.* **2024**, *146* (43), 29742−29750.

(23) Heindel, J. P.; LaCour, R. A.; Head-Gordon, T. The role of charge in microdroplet redox chemistry. *Nat. Commun.* **2024**, *15* (1), No. 3670.

(24) Zhu, C.; Pham, L. N.; Yuan, X.; Ouyang, H.; Coote, M. L.; Zhang, X. High electric fields on water microdroplets catalyze spontaneous and fast reactions in halogen-bond complexes. *J. Am. Chem. Soc.* **2023**, *145* (39), 21207−21212.

(25) Song, Z.; Liang, C.; Gong, K.; Zhao, S.; Yuan, X.; Zhang, X.; Xie, J. Harnessing the high interfacial electric fields on water microdroplets to accelerate menshutkin reactions. *J. Am. Chem. Soc.* **2023**, *145* (48), 26003−26008.

(26) Gong, K.; Nandy, A.; Song, Z.; Li, Q.-S.; Hassanali, A.; Cassone, G.; Banerjee, S.; Xie, J. Revisiting the enhanced chemical reactivity in water microdroplets: the case of a Diels−Alder reaction. *J. Am. Chem. Soc.* **2024**, *146* (46), 31585−31596.

(27) Hao, H.; Leven, I.; Head-Gordon, T. Can electric fields drive chemistry for an aqueous microdroplet? *Nat. Commun.* **2022**, *13* (1), No. 280.

(28) Heindel, J. P.; Hao, H.; LaCour, R. A.; Head-Gordon, T. Spontaneous formation of hydrogen peroxide in water microdroplets. *J. Phys. Chem. Lett.* **2022**, *13* (43), 10035−10041.

(29) Angelaki, M.; Da Silva, Y. C. M.; Perrier, S.; George, C. Quantification and mechanistic investigation of the spontaneous H_2O_2 generation at the interfaces of salt-containing aqueous droplets. *J. Am. Chem. Soc.* **2024**, *146* (12), 8327−8334.

(30) Yang, L.; Liu, Y.; Ge, Q.; Wang, J.; Wang, R.; You, W.; Wang, W.; Wang, T.; Zhang, L. Atmospheric hydroxyl radical route revealed: interface-mediated effects of mineral-bearing microdroplet aerosol. *J. Am. Chem. Soc.* **2025**, *147* (4), 3371−3382.

(31) Wei, Z.; Li, Y.; Cooks, R. G.; Yan, X. Accelerated reaction kinetics in microdroplets: overview and recent developments. *Annu. Rev. Phys. Chem.* **2020**, *71* (1), 31−51.

(32) Chen, H.; Wang, R.; Xu, J.; Yuan, X.; Zhang, D.; Zhu, Z.; Marshall, M.; Bowen, K.; Zhang, X. Spontaneous reduction by one electron on water microdroplets facilitates direct carboxylation with co2. *J. Am. Chem. Soc.* **2023**, *145* (4), 2647−2652.
(33) Yuan, X.; Zhang, D.; Liang, C.; Zhang, X. Spontaneous reduction of transition metal ions by one electron in water microdroplets and the atmospheric implications. *J. Am. Chem. Soc.* **2023**, *145* (5), 2800−2805.
(34) Yan, J.; Zhang, R.; Gao, Y.; Xia, D.; Wu, L.; Yu, Y.; Zhang, H.; Chen, J.; Chen, J.; Francisco, J. S. Spontaneous interfacial redox transformation of 6PPD-Quinone on water microdroplets. *J. Am. Chem. Soc.* **2026**, *148* (16), 17166−17173.
(35) Shirley, J. C.; Ng, Z. X.; Chiang, K.-Y.; Nagata, Y.; Litman, Y.; Hazrah, A. S.; Bonn, M. Reevaluating anomalous electric fields at the air−water interface: a surface-specific spectroscopic survey. *J. Am. Chem. Soc.* **2025**, *147* (50), 46163−46173.
(36) LaCour, R. A.; Heindel, J. P.; Zhao, R.; Head-Gordon, T. The role of interfaces and charge for chemical reactivity in microdroplets. *J. Am. Chem. Soc.* **2025**, *147* (8), 6299−6317.
(37) Purcell, A. G.; Julian, R. R. A critical reappraisal of the evidence for spontaneous generation of hydroxyl radicals in aqueous nanodroplets. *J. Am. Chem. Soc.* **2026**, *148*, 18715−18723.
(38) Asserghine, A.; Baby, A.; N'Diaye, J.; Romo, A. I. B.; Das, S.; Litts, C. A.; Jain, P. K.; Rodríguez-López, J. Dissolved oxygen redox as the source of hydrogen peroxide and hydroxyl radical in sonicated emulsive water microdroplets. *J. Am. Chem. Soc.* **2025**, *147* (14), 11851−11858.
(39) Zhou, J.; Wang, Q.; Cheng, G.; Shen, W.; Zare, R. N.; Sun, X. Charged water microdroplets enable dissociation of surrounding dioxygen. *J. Am. Chem. Soc.* **2025**, *147* (13), 10916−10924.
(40) You, W.; Li, K.; Ge, Q.; Liu, Y.; Wang, W.; Xiong, H.; Ao, J.; Wang, J.; Yang, L.; Wang, R.; Huang, T.; Wang, S.; Liu, H.; Ji, M.; Zhang, L. Breaking the forever bonds: interface-enhanced superoxide chemistry for efficient PFOA degradation. *Environ. Sci. Technol.* **2025**, *59* (35), 19068−19080.
(41) Yang, Y.; Wu, J.; Luo, Z.; Jia, X.; Jiang, G.; Wang, F. Interactions of aqueous microdroplets and mineral particles drive fluorine-first perfluoroalkyl mineralization. *J. Am. Chem. Soc.* **2025**, *147* (36), 32537−32547.
(42) Li, K.; You, W.; Zhu, Y.; Wang, W.; Wang, L.; Ge, Q.; Liu, Y.; Ruan, X.; Cheng, H.; Tahir, M. A.; Zhang, L. Air-water interface of microdroplet enhances photocatalytic oxidative species generation and utilization. *J. Hazard. Mater.* **2025**, *493*, No. 138311.
(43) Krushinski, L. E.; Dick, J. E. Direct electrochemical evidence suggests that aqueous microdroplets spontaneously produce hydrogen peroxide. *Proc. Natl. Acad. Sci. U.S.A.* **2024**, *121* (12), No. e2321064121.
(44) He, J.; Zhao, Q.; Zhang, H.; Xu, Q.; Huang, J.; Shi, X.; Xia, D.; Hou, W.; Chen, J.; Jiang, J.; Xie, H.-B.; Francisco, J. S. Spontaneous reaction between CO_2 and organic acids in water microdroplets: implications for the formation of secondary organic aerosols. *J. Am. Chem. Soc.* **2026**, *148*, 11240−11248.
(45) Li, K.; You, W.; Zhu, Y.; Wang, W.; Wang, L.; Liu, Y.; Ge, Q.; Wang, T.; Wang, R.; Ruan, X.; Cheng, H.; Zhang, L. Strong electric fields on water microdroplets enable near-unity selectivity in H_2O_2 photosynthesis. *J. Am. Chem. Soc.* **2025**, *147* (40), 36136−36145.
(46) Wang, J.; Wolf, R. M.; Caldwell, J. W.; Kollman, P. A.; Case, D. A. Development and testing of a general amber force field. *J. Comput. Chem.* **2004**, *25* (9), 1157−1174.
(47) Rappe, A. K.; Casewit, C. J.; Colwell, K. S.; Goddard, W. A.; Skiff, W. M. UFF, a full periodic table force field for molecular mechanics and molecular dynamics simulations. *J. Am. Chem. Soc.* **1992**, *114* (25), 10024−10035.
(48) Jorgensen, W. L.; Chandrasekhar, J.; Madura, J. D.; Impey, R. W.; Klein, M. L. Comparison of simple potential functions for simulating liquid water. *J. Chem. Phys.* **1983**, *79* (2), 926−935.
(49) Grimme, S.; Antony, J.; Ehrlich, S.; Krieg, H. A consistent and accurate ab initio parametrization of density functional dispersion correction (DFT-D) for the 94 elements H-Pu. *J. Chem. Phys.* **2010**, *132* (15), No. 154104.
(50) VandeVondele, J.; Hutter, J. Gaussian basis sets for accurate calculations on molecular systems in gas and condensed phases. *J. Chem. Phys.* **2007**, *127* (11), No. 114105.
(51) Hartwigsen, C.; Goedecker, S.; Hutter, J. Relativistic separable dual-space gaussian pseudopotentials from H to Rn. *Phys. Rev. B* **1998**, *58* (7), No. 3641.
(52) Neese, F.; Wennmohs, F.; Becker, U.; Riplinger, C. The orca quantum chemistry program package. *J. Chem. Phys.* **2020**, *152* (22), No. 224108.
(53) Weigend, F.; Ahlrichs, R. Balanced basis sets of split valence, triple zeta valence and quadruple zeta valence quality for H to Rn: design and assessment of accuracy. *Phys. Chem. Chem. Phys.* **2005**, *7* (18), 3297−3305.
(54) Lu, T. A comprehensive electron wavefunction analysis toolbox for chemists, multiwfn. *J. Chem. Phys.* **2024**, *161* (8), No. 082503.
(55) Kresse, G.; Furthmüller, J. Efficiency of ab-initio total energy calculations for metals and semiconductors using a plane-wave basis set. *Comput. Mater. Sci.* **1996**, *6* (1), 15−50.
(56) Henkelman, G.; Uberuaga, B. P.; Jónsson, H. A climbing image nudged elastic band method for finding saddle points and minimum energy paths. *J. Chem. Phys.* **2000**, *113* (22), 9901−9904.
(57) Chen, B.; Ni, C.; Ding, L.; Miao, L.; Luo, Z.; Wang, J.; Guo, Y. An iodide-mediated microdroplet for efficient ozone decomposition. *J. Am. Chem. Soc.* **2026**, *148*, 12684−12691.
(58) Chen, Y.; Guo, Z.; Angelaki, M.; Da Silva, Y. C. M.; Song, J.; Wu, W.; Lin, J.; Gandolfo, A.; Chen, J.; George, C. Spontaneous perfluorooctanoic acid degradation at gas−liquid interfaces. *J. Am. Chem. Soc.* **2025**, *147*, 33754−33760.
(59) Eatoo, M. A.; Mishra, H. Disentangling the roles of dissolved oxygen, common salts, and ph on spontaneous hydrogen peroxide production in water: no O_2, no H_2O_2. *J. Am. Chem. Soc.* **2025**, *147* (39), 35392−35400.
(60) Bentel, M. J.; Yu, Y.; Xu, L.; Li, Z.; Wong, B. M.; Men, Y.; Liu, J. Defluorination of per- and polyfluoroalkyl substances (PFASs) with hydrated electrons: structural dependence and implications to PFAS remediation and management. *Environ. Sci. Technol.* **2019**, *53* (7), 3718−3728.
(61) Tomei, G.; Piva, E.; Saleem, M.; Finotto, M.; Pozzebon, M.; Marotta, E. Optimization and testing of an SPE-LC/q-TOF analytical method for the detection of PFAS degradation products in water treatment processes. *Environ. Sci. Technol.* **2025**, *59* (41), 22251−22261.
(62) Jia, X.; Wu, J.; Wang, F. Water-microdroplet-driven interface-charged chemistries. *JACS Au* **2024**, *4* (11), 4141−4147.
(63) Choudhary, A.; Tsunduru, A.; Tsianou, M.; Alexandridis, P.; Bedrov, D. Structure, orientation, and dynamics of per- and polyfluoroalkyl substance (PFAS) surfactants at the air-water interface: molecular-level insights. *J. Colloid Interface Sci.* **2025**, *679*, 1207−1218.
(64) Carter-Fenk, K. A.; Carter-Fenk, K.; Fiamingo, M. E.; Allen, H. C.; Herbert, J. M. Vibrational exciton delocalization precludes the use of infrared intensities as proxies for surfactant accumulation on aqueous surfaces. *Chem. Sci.* **2021**, *12* (24), 8320−8332.
(65) Inerowicz, H. D.; Li, W.; Persson, I. Determination of the transfer thermodynamic functions for some monovalent ions from water to N,N-dimethylthioformamide, and for some anions from water to methanol, dimethyl sulfoxide, acetonitrile and pyridine, and standard electrode potentials of some M+/M(s) couples in N,N-dimethylthioformamide. *J. Chem. Soc., Faraday Trans.* **1994**, *90* (15), 2223−2234.
(66) Hinteregger, E.; Pribil, A. B.; Hofer, T. S.; Randolf, B. R.; Weiss, A. K. H.; Rode, B. M. Structure and dynamics of the chromate ion in aqueous solution. an ab initio QMCF-MD simulation. *Inorg. Chem.* **2010**, *49* (17), 7964−7968.
(67) Dommer, A. C.; Rogers, M. M.; Carter-Fenk, K. A.; Wauer, N. A.; Rubio, P.; Davasam, A.; Allen, H. C.; Amaro, R. E. Interfacial enrichment of lauric acid assisted by long-chain fatty acids, acidity and salinity at sea spray aerosol surfaces. *J. Phys. Chem. A* **2024**, *128* (34), 7195−7207.

(68) Judd, K. D.; Parsons, S. W.; Eremin, D. B.; Fokin, V. V.; Dawlaty, J. M. Visualizing partial solvation at the air−water interface. *Chem. Sci.* **2024**, *15* (22), 8346−8354.
(69) Fried, S. D.; Boxer, S. G. Measuring electric fields and noncovalent interactions using the vibrational stark effect. *Acc. Chem. Res.* **2015**, *48* (4), 998−1006.
(70) Xiong, H.; Lee, J. K.; Zare, R. N.; Min, W. Strong electric field observed at the interface of aqueous microdroplets. *J. Phys. Chem. Lett.* **2020**, *11* (17), 7423−7428.
(71) Foster, M. E.; Wong, B. M. Nonempirically tuned range-separated DFT accurately predicts both fundamental and excitation gaps in DNA and RNA nucleobases. *J. Chem. Theory Comput.* **2012**, *8* (8), 2682−2687.
(72) Wong, B. M.; Hsieh, T. H. Optoelectronic and excitonic properties of oligoacenes: substantial improvements from range-separated time-dependent density functional theory. *J. Chem. Theory Comput.* **2010**, *6* (12), 3704−3712.
(73) Anderson, L. N.; Oviedo, M. B.; Wong, B. M. Accurate electron affinities and orbital energies of anions from a nonempirically tuned range-separated density functional theory approach. *J. Chem. Theory Comput.* **2017**, *13* (4), 1656−1666.
(74) Dai, C.; Li, K.; Liu, Y.; Teng, B.; Chen, Q.; Jin, X.; Xu, D.; Hong, R. Unveiling the directional dynamics: hydrated electron driven defluorination in $PFOA^-$ and $PFOS^-$ through ab initio molecular dynamics and quantum chemistry. *Water Res.* **2025**, *280*, No. 123486.
(75) Shaik, S.; Danovich, D.; Kalita, S.; Dubey, K. D. Oriented electric fields−universal catalysts. *Acc. Chem. Res.* **2025**, *58* (19), 3071−3080.
(76) Wang, Y.; Zhang, J.; Zhang, W.; Yao, J.; Liu, J.; He, H.; Gu, C.; Gao, G.; Jin, X. Electrostatic field in contact-electro-catalysis driven C−F bond cleavage of perfluoroalkyl substances. *Angew. Chem., Int. Ed* **2024**, *63* (19), No. e202402440.

https://doi.org/10.1021/jacs.6c13880
J. Am. Chem. Soc. XXXX, XXX, XXX−XXX